

Tailoring Néel orders in Layered Topological Antiferromagnets

Xiaotian Yang,^{1,2,*} Yongqian Wang,^{3,4,*} Yongchao Wang,⁵ Zichen Lian,⁵
Jinsong Zhang,^{5,6,7} Yayu Wang,^{5,6,7,8} Chang Liu,^{3,4,†} and Wenbo Wang^{1,2,†}

¹*School of Physical Science and Technology, ShanghaiTech University, Shanghai, 201210, China.*

²*ShanghaiTech Laboratory for Topological Physics,
ShanghaiTech University, Shanghai, 201210, China.*

³*School of Physics, Renmin University of China, Beijing, 100872, China.*

⁴*Key Laboratory of Quantum State Construction and Manipulation (Ministry of Education),
Renmin University of China, Beijing, 100872, China.*

⁵*State Key Laboratory of Low Dimensional Quantum Physics, Tsinghua University, Beijing, 100084, China.*

⁶*Frontier Science Center for Quantum Information, Beijing, 100084, China.*

⁷*Hefei National Laboratory, Hefei, 230088, China.*

⁸*New Cornerstone Science Laboratory, Frontier Science Center for Quantum Information, Beijing, 100084, China.*

In the two-dimensional limit, the interplay between Néel order and band topology in van der Waals topological antiferromagnets can give rise to novel quantum phenomena in the quantum anomalous Hall state, including the cascaded quantum phase transition and spin-modulation effect[1–5]. However, due to the absence of net magnetization in antiferromagnets, probing the energetically degenerate Néel orders has long remained a significant challenge. Inspired by recent advances in realizing the quantum anomalous Hall effect in AlO_x -capped layered topological antiferromagnet MnBi_2Te_4 [5–7], we demonstrate deterministic control over the Néel order through surface anisotropy engineering enabled by the AlO_x capping layer. By tuning the surface anisotropy, we uncover parity-dependent symmetry breaking states that manifest as distinct odd-even boundary architectures, including 180° domain walls or continuous spin structures. Comparative studies between AlO_x -capped and pristine odd-layer MnBi_2Te_4 flakes using domain-resolved magnetic force microscopy reveal pronounced differences in coercivity and magnetization-reversal dynamics. Notably, an unconventional giant exchange bias, which arises from perpendicular magnetic anisotropy rather than traditional interface pinning mechanisms, is observed for the first time. Our findings establish a pathway for manipulating Néel order through surface modification in A-type antiferromagnets, offering new opportunities for spintronic devices and quantum information technologies.

A-type antiferromagnetic materials exhibit a dual magnetic character defined by intralayer ferromagnetic coupling and interlayer antiferromagnetic interactions[8–17]. This unique magnetic order manifests distinct layer-parity-dependent phenomena in few-layer thin flakes:

even-layer systems with zero net moment behave as conventional antiferromagnets, whereas odd-layer configurations retain a net magnetic moment akin to ferromagnets. As the first experimentally identified layered antiferromagnet with nontrivial band topology, MnBi_2Te_4 (MBT) family materials offer a versatile platform to explore the intricate interaction among dimensionality, topology and antiferromagnetism. In MBT, the parity-dependent magnetism is directly coupled to its topological electronic states. Even-layer systems stabilize axion insulator phases[18–20], while odd-layer counterparts host quantum anomalous Hall (QAH) states[1–4]. Precise manipulation of magnetic spin states has become essential for topological systems, given their direct correlation with topological invariants[21–27]. However, the magnetic ground state of A-type antiferromagnets comprises a two-fold degeneracy between antiparallel Néel orders, which is difficult to detect in conventional magnetic measurements. For odd-layer systems, the Néel vector aligns with the net magnetization, enabling strong coupling to external magnetic fields. In contrast, even-layer systems without net magnetization exhibit field-insensitive Néel orders, making it challenging to artificially control the Néel states.

Recent advances in interfacial engineering, such as AlO_x capping of MnBi_2Te_4 surfaces, suggest a pathway to address this challenge. AlO_x contact with either surface of MBT significantly amplifies the anomalous Hall effect toward full quantization, likely attributed to the enhanced surface perpendicular magnetic anisotropy (PMA)[1, 5–7, 28]. This interfacial engineering strategy, which involves coating magnetic systems with amorphous oxide capping layers to stabilize PMA, has been experimentally implemented in diverse systems[29–31]. In pristine MBT systems, surface magnetic parameters—including magnetic moment, exchange coupling, and magnetic anisotropy—are typically weaker than those in the bulk[32]. This disparity manifests as multiple-step metamagnetic transitions during magnetization reversal[33, 34]. Capping a layer of AlO_x can enhance surface PMA, potentially surpassing even the bulk PMA (Fig. 1a). This effect effectively pins the surface spin

* These authors contribute equally to this work.

† Corresponding authors:

liuchang.phy@ruc.edu.cn, wangwb1@shanghaitech.edu.cn

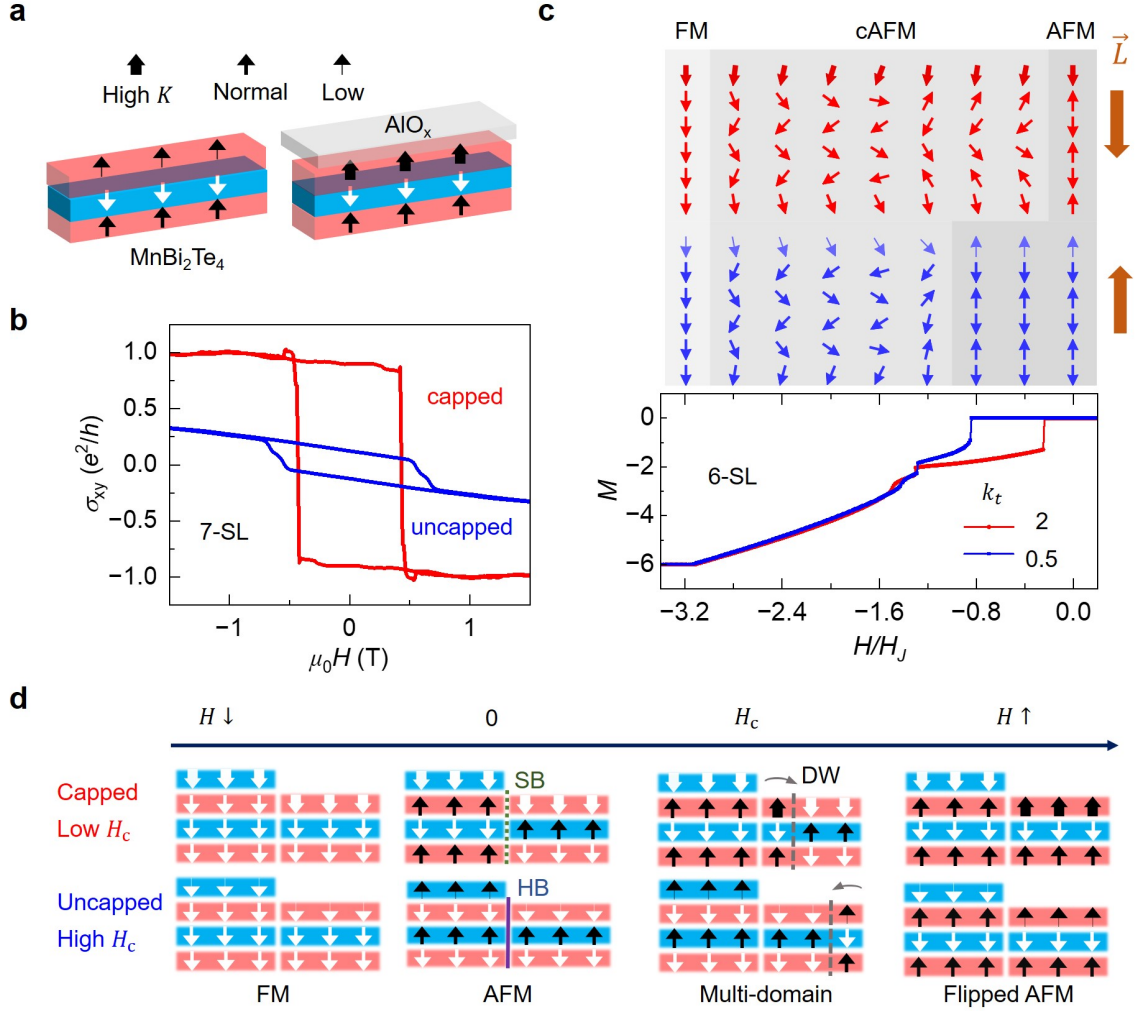


FIG. 1. Néel orders of AlO_x -capped and pristine MBT thin flakes **a**, Schematic representation of enhanced (thicker arrows) and suppressed (thinner arrows) surface magnetic anisotropy in AlO_x -capped and pristine MnBi_2Te_4 . **b**, Field-dependent Hall conductance (σ_{xy}) of capped (1.5 K) and uncapped (2 K) 7-SL MnBi_2Te_4 at charge neutral points. **c**, Simulated spin reorientations for 6-SL systems upon field removal, showing metamagnetic transition from ferromagnetic (FM) to canted-antiferromagnetic (cAFM) to antiferromagnetic (AFM) phases. Red spins are for enhanced surface anisotropy ($k_t = 2$), while blue ones are for suppressed surface anisotropy ($k_t = 0.5$). The Néel vectors \vec{L} of the AFM ground states at zero fields show opposite directions. Corresponding M - H curves are plotted in lower panel. **d**, Schematic illustrations of the magnetization reversal process of odd-even staircases for enhanced (capped) and suppressed (uncapped) surface anisotropy. The magnetically soft and hard OEBs are labelled as SB and HB, respectively, resulting in lower and higher coercive field (H_c). The domain wall (DW) propagation directions differ between these two cases.

direction, enabling deterministic control over the Néel orders in even-layer systems.

In this study, we introduce a methodology to determine and manipulate Néel orders in A-type antiferromagnets through surface modification. In AlO_x -capped and pristine MnBi_2Te_4 thin flakes, the odd-even boundaries (OEB) exhibit distinct magnetic properties during magnetization reversal, indicating inverted Néel orders in the even-layer regions. The unique coercivity of OEBs can be leveraged to design giant exchange bias effects in odd-layer thin flakes. This design strategy extends beyond MnBi_2Te_4 systems and is applicable to other A-type van

der Waals antiferromagnets, offering a versatile approach for controlling antiferromagnetic states in layered materials.

Transport and calculated Néel orders

To validate the role of AlO_x capping, we fabricated both AlO_x -capped and pristine MnBi_2Te_4 thin flakes and systematically characterized their Hall conductances. At 1.5 K, the σ_{xy} - H loops for AlO_x -capped 7-septuple-layer (7-SL) devices exhibit square-like hysteretic be-

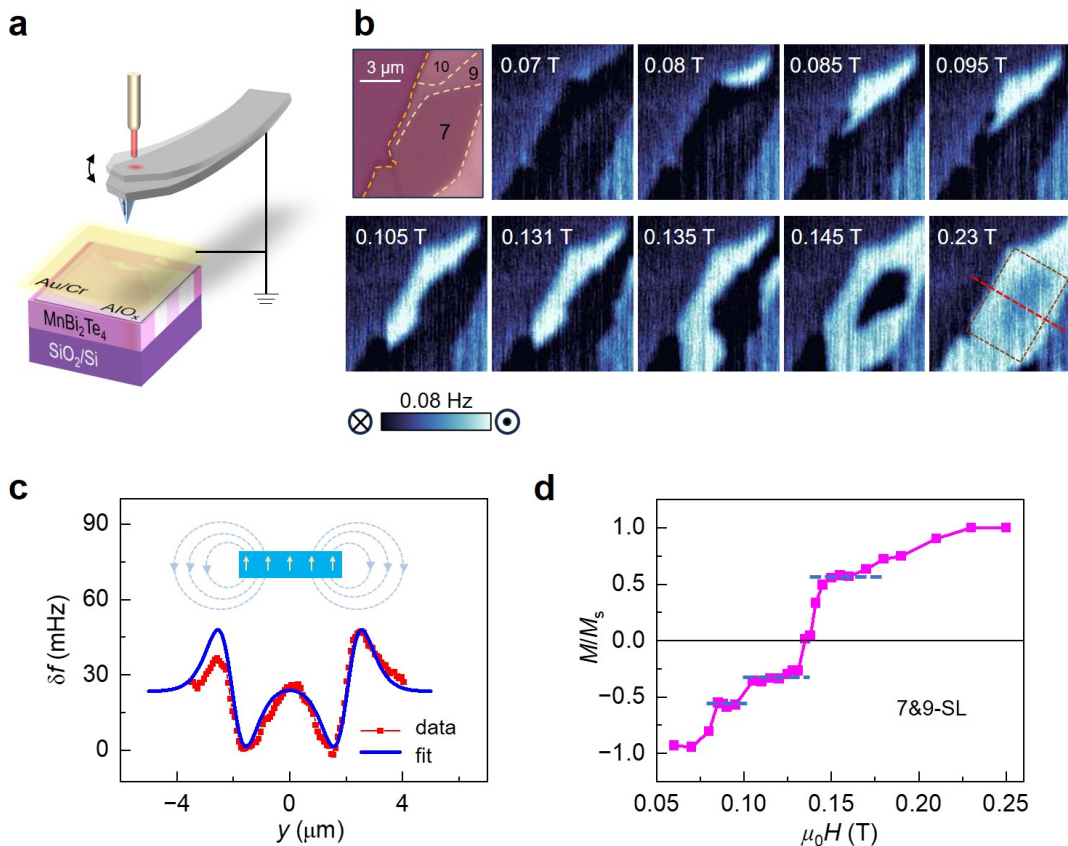


FIG. 2. **Robust A-type antiferromagnetism in MBT thin flakes.** **a**, Schematic illustration of MFM setup based on interferometer sensors, scanning on AlO_x -capped MnBi_2Te_4 staircases. The sample was coated with Cr and Au metals, which was utilized as electrode to balance electric potential between the magnetic tip and sample surface. **b**, MFM measurements on AlO_x -capped MnBi_2Te_4 thin flakes at various magnetic fields. The sample edge is marked by yellow dashed lines, while atomic steps on the thin flake are outlined by light-yellow dashed lines. The number of SLs is labelled on the corresponding terraces. **c**, Line profile (red dashed line) of the MFM images at 0.23 T, which can be accurately fitted by the dipole field from a uniformly magnetized rectangular sheet (yellow dashed rectangle). **d** Normalized magnetization of even-SL thin flakes, deduced from MFM images at various fields, exhibits Barkhausen effect. Small magnetization plateaus are indicated by blue dashed lines.

behavior with a zero-field Hall conductance reaching approximately $0.90e^2/h$, approaching the quantum anomalous Hall (QAH) state, as illustrated in Fig. 1b. The temperature dependence of the anomalous Hall conductance aligns well with the mean-field theory for a Landau second-order phase transition, described by $\sigma_{xy} \propto (T_N - T)^{0.5}$, where $T_N \approx 22.0\text{K}$, highlighting the robustness of A-type antiferromagnetic ordering[35, 36]. In contrast, the uncapped flake shows a significantly lower anomalous Hall conductance, consistent with prior findings that suggest AlO_x capping enhances PMA[6, 7].

A linear-chain model was employed to calculate how surface magnetic anisotropy modifies the spin states at various magnetic fields (methods)[37–40]. Each layer was treated as a homogeneous macro moment \mathbf{m} . The hysteretic metastable states were determined by minimizing the total magnetic free energy, which includes contributions from Zeeman energy, PMA energy, and inter-layer antiferromagnetic exchange energy. At high nega-

tive fields, all moments align downward, forming a ferromagnetic (FM) state. As the field is reduced to zero, the system transitions through a canted antiferromagnetic (cAFM) state and finally reaches the antiferromagnetic (AFM) ground state. The Néel vectors of the AFM ground states are defined as $\mathbf{L} = \mathbf{m}_1 - \mathbf{m}_2$, where \mathbf{m}_1 and \mathbf{m}_2 represent the macro moment of the surface and subsurface layer, respectively. During the metamagnetic transition of even-SL systems, enhanced surface PMA pins the spin orientation of the topmost layer, thereby stabilizing an AFM ground state with a downward Néel vector at zero field. Conversely, suppressed surface PMA triggers spin reorientation in the surface layer, ultimately stabilizing an upward Néel vector. As shown in Fig. 1c, a doubled surface anisotropy in 6-SL flake results in a $\downarrow\uparrow\downarrow\uparrow\downarrow$ moment sequence (red), while halved surface anisotropy yields $\uparrow\downarrow\uparrow\downarrow$ (blue). In contrast, odd-SL flakes, regardless of the surface anisotropy, exhibits the identical AFM states, such as $\downarrow\uparrow\downarrow\downarrow$, en-

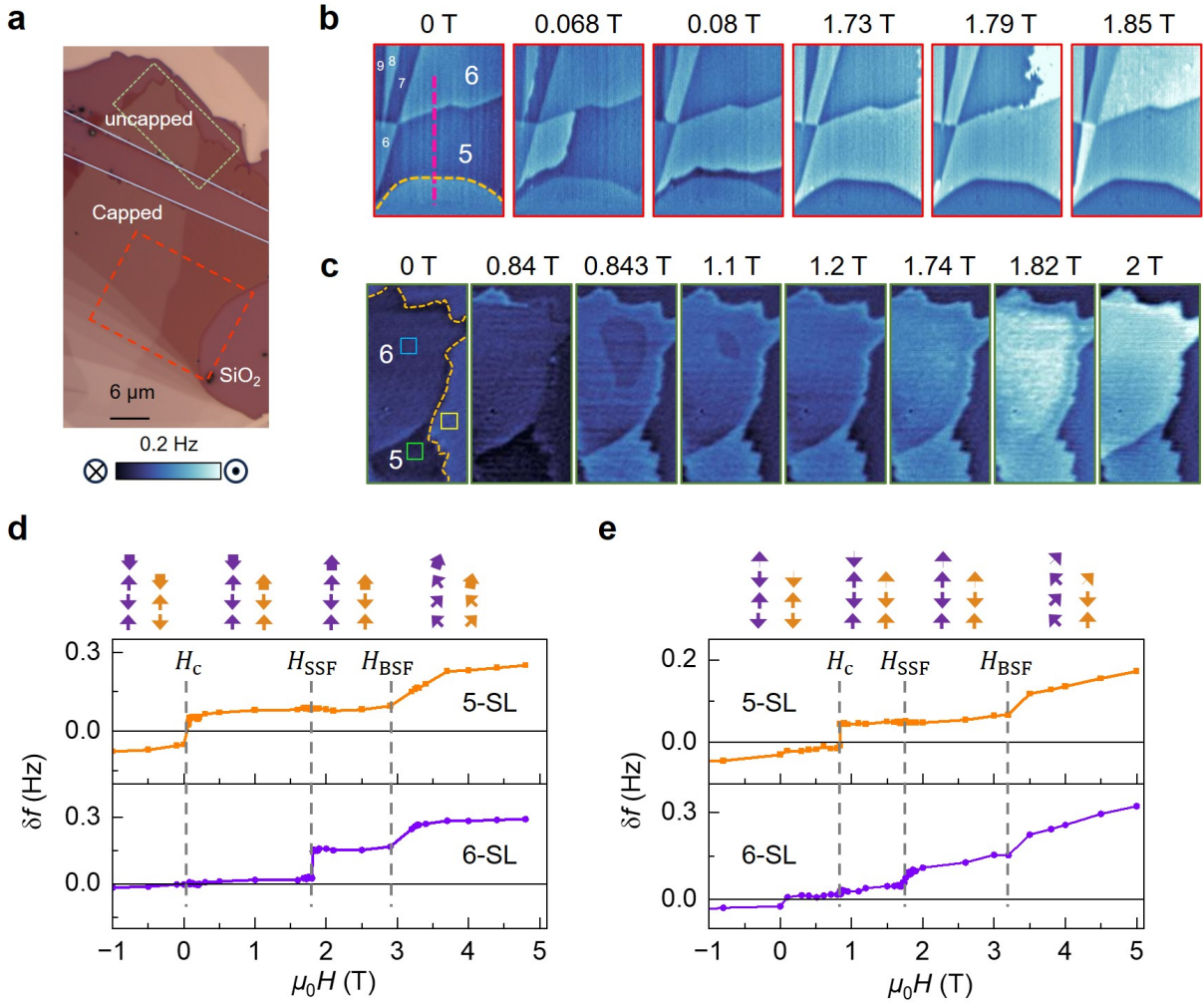


FIG. 3. **Distinct magnetization reversal processes of capped and pristine MBT thin flakes.** **a**, Optical image of the AlO_x -capped and uncapped MBT from the same specimen. The scratch separating capped and uncapped regions are labelled by blue solid lines, and the MFM scanning areas are marked by red and green dashed lines. **b**, MFM images of capped MBT at various magnetic fields. The flake edge is outlined by yellow dashed lines. **c**, MFM images of uncapped MBT at various magnetic fields. **d**, MFM signals of 5- and 6-SL capped MBT, derived from the domain contrast along the line profile shown in **b**. **e**, MFM signals of 5- and 6-SL uncapped MBT, derived from the domain contrast within the square areas shown in **c**. Critical magnetic fields for different magnetic phases are indicated by gray dashed lines. H_c , H_{SSF} and H_{BSF} represent the coercive field of 5-SL, the surface-spin-flip field of 6-SL, the bulk-spin-flop field of both thin flakes. The schematic spin structures corresponding to each magnetic phase are illustrated at the top of the graphs.

ensuring a net downward magnetization during metamagnetic transitions. Consequently, OEBs exhibit distinct magnetic properties at zero fields. Enhanced surface anisotropy results in a 180° domain wall, while reduced surface anisotropy maintains coherent spin continuity. When a positive field is applied, the Néel vector of odd-SL flakes flips, transitioning from $\downarrow\uparrow\downarrow$ to $\uparrow\downarrow\uparrow$. The magnetization reversal processes at these two types of OEBs differ significantly (Fig. 1d). For a 180° domain wall, reversal occurs through domain-wall propagation without domain nucleation. In capped MBT, magnetization switching initiates at OEBs, and the coercivity is negligible if domain-wall pinning is weak. This OEB is termed a mag-

netically soft boundary (SB), which is marked by green vertical dashed line in Fig. 1d. Conversely, uncapped flakes tend to form a single-domain state with continuous spin structures across the OEB, representing a magnetically hard boundary (HB, marked by purple vertical solid line), which makes magnetization switching energetically unfavorable. Domain switching in this case requires overcoming a domain nucleation barrier, which scales with magnetic anisotropy energy K [41, 42]. Consequently, domain switching in uncapped flakes initiates at sample edges or involves coherent spin flipping in the absence of domain formation. Theoretically, the coercivity difference between these two scenarios is $\mu_0 \Delta H_c \approx K/M_s$,

where M_s is the saturation magnetization.

Domain behavior during spin flips

In order to experimentally verify this prediction, we utilized cryogenic magnetic force microscopy (MFM) to probe the magnetic domain evolutions at various magnetic fields (Fig. 2a). Magnetic imaging was first performed on AlO_x -capped MBT thin flakes, focusing on the 7-SL terrace, where QAHE has been realized. The thin flake had been magnetically saturated at negative fields, then the field was removed and ramped to positive. The magnetization reversal process of the odd-layer terraces exhibits a typical ferromagnetic domain behavior with domain wall propagation, as shown in Fig. 2b. At 0.08 T, up domains started to nucleate from the 9-/10-SL boundary and domain wall propagated into the 7-SL region. The magnetization switching gradually occurred at the edges of the 7-SL terrace, with the center area unswitched at 0.145 T. Domain patterns exhibit remarkable stability across the field intervals of 0.085~0.095 T and 0.105~0.131 T, due to domain wall pinning effects. The odd-SL area was completely switched at 0.23 T. A line cut across the 7-SL terrace reveals the local dependence of the MFM signals, given by $\delta f \propto \frac{d^2 B_z}{dz^2}$ for a magnetic dipole tip[43]. The magnetic field B_z generated by a ferromagnetic thin flake with PMA is analogous to the electric field outside a parallel capacitor. The dipole field can be derived from the scalar potential ϕ : $B_z \propto -\frac{d\phi}{dz}$. For a rectangular thin flake the scalar potential across the midline of the long edge can be expressed as $\phi(z) \propto \arctan \frac{L(W-2y)}{2z\sqrt{L^2+(W-2y)^2+4z^2}} + \arctan \frac{L(W+2y)}{2z\sqrt{L^2+(W+2y)^2+4z^2}}$, where $L = 5.1 \mu\text{m}$, $W = 4.1 \mu\text{m}$ are respectively the length and width of the rectangle[44]. As shown in Fig. 2c, the line profile can be nicely fitted by this model at $z = 1.2 \mu\text{m}$, suggesting the effective lift height of the tip dipole moment. This consistency indicates the homogeneous magnetization in the MBT thin flake. By calculating the switched areas, the normalized magnetization M/M_s can be estimated at various fields. Fine magnetization plateaus and Barkhausen jumps are evident on the magnetization switching curve in Fig. 2d, highlighting robust intralayer ferromagnetic ordering[45, 46]. This magnetization reversal process starkly contrasts with other QAH systems, including magnetically doped topological insulator films[47, 48], MBT films[49] and twisted bilayer systems[50, 51], where disordered magnetic domains or even superparamagnetic behaviors have been visualized, indicating magnetic inhomogeneity.

To directly compare the impact of AlO_x capping on surface magnetism, we cleaved another MBT thin flake containing regions of varying thicknesses. Half of the flake was capped with a 3 nm AlO_x layer, with the AlO_x boundary intentionally aligned across the interface between 5- and 6-SL regions (Fig. 3a). The flake was then mechanically split along the AlO_x boundary using a sharp needle. Subsequent MFM imaging was performed on both AlO_x -capped and uncapped 5- and 6-SL regions. In capped regions, magnetization reversal initiated in the 5-SL segment at 0.068 T, with domain nucleation observed precisely at the 5-/6-SL boundary (Fig. 3b), analogous to previous reversal dynamics in 7-SL systems. Upon increasing the field to 1.73 T, the 6-SL region underwent magnetization reversal, attributed to surface spin flip (SSF), accompanied by domain formation. The propagation from right to left of the magnetic domain walls stems from the presence of an AlO_x capping boundary at the right edge of the sample. This directional motion provides direct evidence that 6-SL SSF transitions nucleate preferentially within uncapped regions, where reduced surface PMA lowers the energy barrier for spin flips. At 1.85 T, the SSF transition in the 6-layer region completed, and further field increases triggered bulk magnetization reversal in both 6- and 5-SL regions. Notably, this bulk spin flip (BSF) occurred without observable domain nucleation, suggesting a coherent spin-flop process across the entire lattice. By analyzing the MFM signal contrast between the 5-/6-SL and the 5-SL/substrate boundaries, we reconstructed layer-resolved magnetic hysteresis curves. These curves reveal distinct critical fields: $\mu_0 H_c \approx 0.068$ T for 5-SL spin flip, $\mu_0 H_{\text{SSF}} \approx 1.80$ T for 6-SL SSF, and $\mu_0 H_{\text{BSF}} \approx 2.90$ T for BSF in both SLs (Fig. 3d). In contrast, uncapped flakes exhibit no magnetization reversal below 0.84 T. At 0.843 T, abrupt spin-flip transitions occur: complete reversal in the 5-SL and partial reversal in the 6-SL, leaving a metastable unswitched core (Fig. 3c). This behavior starkly contrasts with AlO_x -capped systems. The absence of domain nucleation at the 5-/6-SL boundary and the monodomain-like reversal pathway in entire uncapped flakes imply spontaneous single-domain formation at zero field, consistent with theoretical predictions of reduced surface PMA. Such layer-sharing spin-flip transition was also visualized in few-layer CrSBr systems with in-plane magnetic anisotropy[52]. The disparity between capped and uncapped systems $\mu_0 \Delta H_c \approx 0.77$ T enables quantitative estimation of nucleation energy barrier. Nucleation energy barrier per Mn ion equals $\mu_0 H_c \mu_{\text{Mn}} \approx 0.205$ meV, given Mn ion moment $\mu_{\text{Mn}} \approx 4.61 \mu_B$. This value is comparable with the theoretical magnetic anisotropy energy 0.225 meV from first-principle calculations[12]. This layer-parity-dependent phenomenon was further validated in a separate sample at the 7-/8-SL boundary. In AlO_x -capped regions, magnetization reversal nucleates preferentially at the 7-/8-SL boundary, whereas in uncapped regions, reversal initiates at the 7-SL flake edge. Furthermore, these two configura-

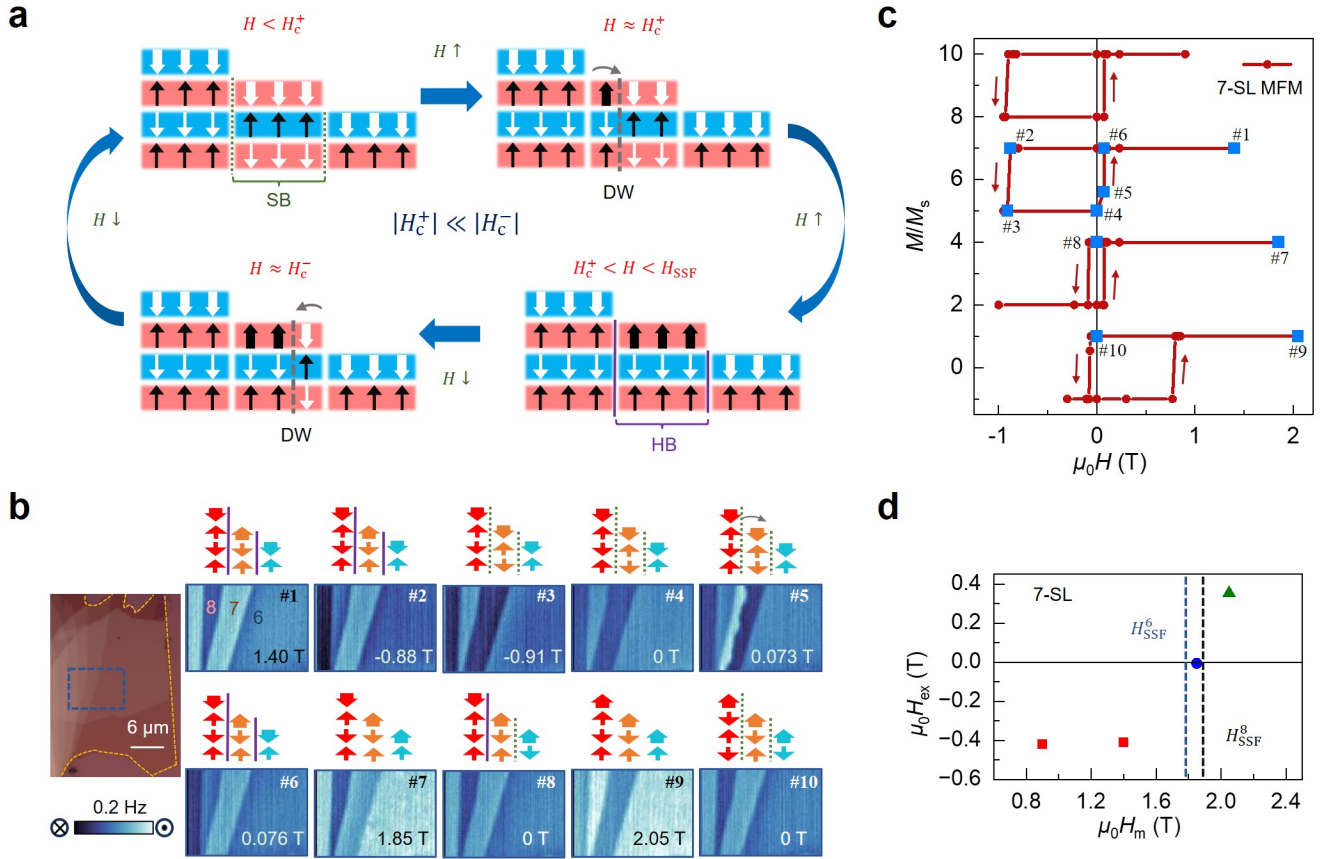


FIG. 4. **Giant exchange bias in odd-SL MBT encircled by even-SL terraces** **a**, Schematic diagrams of exchange bias effect in 2-/3-/4-SL staircase structures, when the applied field is below the surface-spin-flip field (H_{SSF}) of the even-SL. The SBs, HBs, DWs are labelled by green dashed, purple solid and gray dashed lines, respectively. The positive coercive field (H_c^+) is much smaller than negative one (H_c^-). **b**, Optical image of the thin flake with its edges outlined by yellow dashed lines. MFM scanning area is highlighted by blue dashed lines. MFM images of 6-/7-/8-SL staircase structure at various magnetic fields (#1-10). The corresponding spin structures are illustrated at top. **c**, Magnetization curves of 7-SL MBT derived from MFM images exhibit exchange bias effect. Red circles are data points from MFM images. Blue squares correspond to the representative MFM images shown in **b**. The red arrows represent the field-sweeping directions. **d**, Exchange fields H_{ex} for distinct maximum positive fields (H_m) demonstrate strong correlation with the spin states of neighboring even-SL regions. H_{SSF}^6 and H_{SSF}^8 denote surface-spin-flip fields for 6-SL and 8-SL terraces, respectively.

rations exhibit an order-of-magnitude disparity in coercive fields. These findings conclusively demonstrate that AlO_x capping amplifies surface PMA, stabilizing zero-field domain walls at OEBs.

Giant exchange bias effect

The stark layer-parity dependence of coercive fields enables the design of giant EB effect through tailored multilayer antiferromagnetic architectures, as illustrated in Fig. 4a. Consider a central odd-layer terrace (e.g., 3-SL) flanked by even-layer regions (4- and 2-SL), forming a stepped structure. During field cycling from high negative fields to zero, spin configurations evolve as follows: The 4-3 and 3-2 boundaries initially act as SBs, permitting low-energy magnetization switching. The magneti-

zation reversal prefers to initiate at the 4-3 OEBs, because the domain wall depinning at 3-2 OEBs requires the extension of domain walls which costs additional energy. Upon magnetization reversal of the 3-SL, from $\downarrow\uparrow\downarrow$ to $\uparrow\downarrow\uparrow$, these OEBs transform into HBs, requiring substantially higher negative fields to reverse the 3-SL magnetization—a hallmark of layer-correlated exchange bias. To validate this mechanism, we probed magnetization reversal in AlO_x -capped 6-/7-/8-SL staircase. The thin flakes were initially polarized at -5 T. The field consequently were swept back and forth to obtain the M - H loops for 7-SL. The maximum positive fields H_m were increasing for each loop. For $H_m = 0.90$ and 1.40 T, lower than the even-layer H_{SSF} , a constant exchange bias field was yielded in 7-SL $H_{EB} \approx -0.41$ T. The magnetization reversal processes for $H_m = 1.40$ T were shown in Fig. 4c-h. The field was firstly cycled to

1.40 T, reversing the field leads to magnetization switching around $H_c^- \approx -0.90$ T (Fig. 4d,e). The magnetization reversal at positive field was order-of-magnitude smaller (Fig. 4g,h). Domain switching was visualized at $H_c^+ \approx 0.073$ T from 7-/8-SL OEBs. At 1.85 T, the 6-SL surface flips while the 8-SL remains unchanged. Removing the field creates asymmetric boundaries: a soft 6-/7-SL boundary and a hard 7-/8-SL boundary (Fig. 4j). This configuration reduces both positive and negative coercive fields ($H_c^- = -0.085$ T, $H_c^+ = 0.074$ T), as either magnetization state benefits from one soft nucleation boundary, effectively nullifying H_{EB} . Finally, at 2.05 T, 8-SL SSF resets the system to its initial symmetric OEB configuration (Fig. 4l) but with inverted EB polarity $H_{EB} \approx 0.36$ T, as shown in Fig. 4m. Analogous EB effect with comparable H_{EB} were experimentally resolved in adjacent 9-SL regions, attributing their origin to PMA rather than thickness-dependent bulk interactions. The tight correlation between odd-SL H_{EB} and even-SL spin states unambiguously attributes this EB effect to OEBs. This observed EB mechanism is fundamentally distinct from previously reported effects in MBT. Earlier reports attributed exchange bias to defect-mediated spin pinning and inhomogeneous magnetic interactions within odd-SL regions[40, 53, 54]. In MBT, where the topological Chern number sign is governed by magnetization orientation, this layer-parity-mediated exchange bias offers a deterministic pathway to tailor topological edge states.

In summary, we introduce a methodology to resolve and manipulate Néel orders in A-type antiferromagnets by analyzing domain-reversal processes at parity-engineered layer boundaries. In systems where surface PMA is enhanced or suppressed, parity boundaries exhibit orders-of-magnitude differences in coercive fields, serving as a magnetic fingerprint for surface spin re-configuration. In AlO_x -capped MBT, this principle enables giant exchange bias effects (~ 0.4 T) in odd-layer terraces. Critically, this layer-parity-engineering strategy can be extended to other A-type van der Waals antiferromagnets by artificially constructing OEBs. Unlike conventional exchange bias mechanisms, which rely on interfacial pinning in ferromagnet/antiferromagnet heterostructures and are influenced by extrinsic factors such as interface roughness and grain size, our approach leverages intrinsic parity boundaries in A-type antiferromagnetic single crystals. These naturally occurring OEBs allow for precisely tunable bias fields in odd-layer systems by manipulating the magnetic states of even-layer neighbors. Furthermore, exchange bias magnitudes, which scale with PMA, can be tailored through surface anisotropy modulation, offering a pathway to design non-volatile spin-texture memories and topological quantum devices.

METHODS

Device fabrication

Few-layer MnBi_2Te_4 flakes were mechanically exfoliated onto 285-nm-thick SiO_2/Si substrates using the Scotch tape method in an Ar-filled glovebox, maintaining O_2 and H_2O levels below 0.1 ppm. To ensure a clean surface and enhance adhesion, the substrates were sequentially cleaned with acetone, isopropanol, and deionized water, followed by air plasma treatment at 125 Pa for 3 min. To achieve selective AlO_x coverage, a physical mask was placed over the MnBi_2Te_4 flakes before aluminum deposition to partially shield specific regions. Aluminum was thermally evaporated at a deposition rate of 0.04 nm/s under a vacuum better than 4×10^{-4} Pa, followed by oxidation in an oxygen atmosphere at a pressure of 2×10^{-2} Pa for 5 min to form a 3-nm-thick AlO_x layer in the exposed areas. After oxidation, the mask was removed, and the sample was then mechanically separated using a sharp needle to create two distinct regions with and without AlO_x capping layer. To balance the electrostatic potential for subsequent MFM measurements, a Cr/Au (3/25 nm) layer was deposited via thermal evaporation, ensuring uniform electrical contact across both regions and minimizing electrostatic artifacts that could interfere with magnetic imaging.

Transport measurements

Four-probe transport measurements were performed in a cryogenic system operating at a base temperature of 1.5 K, with an out-of-plane magnetic field up to 9 T. An AC current of 100 nA at 13 Hz, generated by a Keithley 6221 current source, was applied to the sample, and the longitudinal and Hall voltage were simultaneously detected using lock-in amplifiers (Stanford Research Systems SR830). To correct for geometric misalignment, the longitudinal and Hall signals were symmetrized and anti-symmetrized with respect to the applied magnetic field. The back-gate voltage was controlled via a Keithley 2400 source meter through the SiO_2/Si substrate.

Linear-chain model calculations

In A-type antiferromagnetic materials, we can regard i th layer as a macro moment \mathbf{m}_i . For homogeneous macro-moment size, we can set $|\mathbf{m}_i| = 1$ for simplicity. The total magnetic free energy of N-SL MnBi_2Te_4 can be written as

$$E = -H \sum_{i=1}^N \cos \theta_i + H_K (\sum_{i=2}^N \sin^2 \theta_i + k_t \sin^2 \theta_1) + H_J \sum_{i=1}^{N-1} \cos(\theta_i - \theta_{i+1}) \quad (1)$$

where H is magnetic field along z axis and θ_i is the angle between \mathbf{m}_i and z axis. These three terms correspond to

Zeeman energy, PMA energy ($H_K > 0$) and interlayer antiferromagnetic exchange energy ($H_J > 0$), respectively. k_t term represents the coefficient of the surface PMA. For MBT, we set $H_K/H_J = 0.3$ [38]. The spin orientations $\{\theta_i\}$ therefore can be determined by searching for the nearest local minimum evolving from the previous state. In *mathematica*, we utilized *FindMinimum* to efficiently find the local minimum of total free energy. The magnetization curve can be obtained by calculating $M = \sum_{i=1}^N \cos \theta_i$.

MFM measurements

Cryogenic MFM experiments were conducted in a commercial atomic force microscope (atto-AFM) equipped with commercial cantilevers (spring constant $k \approx 2.8$ N/m and resonance frequency ≈ 75.8 kHz) in a closed-cycle helium cryostat. The tip deflections were detected by an all-fiber low-coherence interferometer. An out-of-plane magnetic field was applied using a superconducting magnet. MFM images were taken in a constant height mode with lift height of ~ 200 nm. MFM signal, the change of cantilever resonance frequency, is proportional to the gradient of out-of-plane stray field. Electrostatic interaction was minimized by balancing the tip-surface potential difference. To avoid the relaxation effect (domain wall creeping) during the spin-flip transitions of odd-SL MBT near H_c and to minimize the stray field effect of the MFM tips, all MFM images were taken at a low magnetic field of approximately 0.03 T after the magnetic field was ramped to the desired values.

Acknowledgements We thank Y. Chen and Z. Zhu for discussions. Wenbo Wang was sponsored by National Key Research and Development Program of China (Grant No. 2022YFA1403000), and National Natural Science Foundation of China (Grant No. 12374161). Yayu Wang was supported by the Basic Science Center Project of Natural Science Foundation of China (Grant No. 52388201), the Innovation program for Quantum Science and Technology (Grant No. 2021ZD0302502) and the New Cornerstone Science Foundation through the New Cornerstone Investigator Program and the XPLOER PRIZE. Chang Liu was supported by the National Natural Science Foundation of China (Grant No. 12274453); Beijing Nova Program (Grant No. 20240484574). Jin-song Zhang was supported by the National Natural Science Foundation of China (Grant Nos. 12274252 and 12350404).

Author contributions W.B.W conceived the project. W.B.W., Y.Y.W, C.L and J.S.Z supervised the research. Y.C.W. synthesized the MnBi_2Te_4 single crystals. Y.Q.W. and Z.C.L. fabricated the devices and performed the transport measurements. X.T.Y. and W.B.W performed the MFM experiments and analyzed the data.

W.B.W. performed the linear-chain model calculations. W.B.W. and X.T.Y. wrote the manuscript. All authors discussed the data and contributed to the manuscript.

- [1] Deng, Y. *et al.* Quantum anomalous Hall effect in intrinsic magnetic topological insulator MnBi_2Te_4 . *Science* **367**, 895–900 (2020).
- [2] Fu, H., Liu, C.-X. & Yan, B. Exchange bias and quantum anomalous Hall effect in the $\text{MnBi}_2\text{Te}_4/\text{CrI}_3$ heterostructure. *Sci. Adv.* **6**, eaaz0948 (2020).
- [3] Li, H., Chen, C.-Z., Jiang, H. & Xie, X. C. Coexistence of quantum Hall and quantum anomalous Hall phases in disordered MnBi_2Te_4 . *Phys. Rev. Lett.* **127**, 236402 (2021).
- [4] Bai, Y. *et al.* Quantized anomalous Hall resistivity achieved in molecular beam epitaxy-grown MnBi_2Te_4 thin films. *Natl. Sci. Rev.* **11**, nwad189 (2023).
- [5] Lian, Z. *et al.* Antiferromagnetic quantum anomalous Hall effect modulated by spin flips and flops. *arXiv: 2405.08686* (2024).
- [6] Li, Y. *et al.* Fabrication-induced even-odd discrepancy of magnetotransport in few-layer MnBi_2Te_4 . *Nat. Commun.* **15**, 3399 (2024).
- [7] Wang, Y. *et al.* Towards the quantized anomalous Hall effect in AlO_x -capped MnBi_2Te_4 . *Nat. Commun.* **16**, 1727 (2025).
- [8] May, S. J. *et al.* Enhanced ordering temperatures in antiferromagnetic manganite superlattices. *Nat. Mater.* **8**, 892–897 (2009).
- [9] Baltz, V. *et al.* Antiferromagnetic spintronics. *Rev. Mod. Phys.* **90**, 015005 (2018).
- [10] Gong, S.-J. *et al.* Electrically induced 2D half-metallic antiferromagnets and spin field effect transistors. *Proc. Natl. Acad. Sci.* **115**, 8511–8516 (2018).
- [11] Jiang, S., Li, L., Wang, Z., Mak, K. F. & Shan, J. Controlling magnetism in 2D CrI_3 by electrostatic doping. *Nat. Nanotechnol.* **13**, 549–553 (2018).
- [12] Otrokov, M. M. *et al.* Prediction and observation of an antiferromagnetic topological insulator. *Nature* **576**, 416–422 (2019).
- [13] Yan, J.-Q. *et al.* A-type antiferromagnetic order in MnBi_4Te_7 and $\text{MnBi}_6\text{Te}_{10}$ single crystals. *Phys. Rev. Mater.* **4**, 054202 (2020).
- [14] Rahman, S., Torres, J. F., Khan, A. R. & Lu, Y. Recent developments in van der Waals antiferromagnetic 2D materials: synthesis, characterization, and device implementation. *ACS Nano* **15**, 17175–17213 (2021).
- [15] Ye, C. *et al.* Layer-dependent interlayer antiferromagnetic spin reorientation in air-stable semiconductor CrSBr . *ACS Nano* **16**, 11876–11883 (2022).
- [16] Schruck, B. *et al.* Emergence of Fermi arcs due to magnetic splitting in an antiferromagnet. *Nature* **603**, 610–615 (2022).
- [17] Chen, X. *et al.* Antiferromagnetic order in the layered magnetic topological insulator MnBi_2Se_4 probed by resonant soft x-ray scattering. *Phys. Rev. B* **109**, 184418 (2024).
- [18] Zhang, D. *et al.* Topological axion states in the magnetic insulator MnBi_2Te_4 with the quantized magnetoelectric effect. *Phys. Rev. Lett.* **122**, 206401 (2019).
- [19] Li, J. *et al.* Intrinsic magnetic topological insulators in van der Waals layered MnBi_2Te_4 -family materials. *Science Advances* **5**, eaaw5685 (2019).
- [20] Liu, C. *et al.* Robust axion insulator and Chern insulator phases in a two-dimensional antiferromagnetic topological insulator. *Nat. Mater.* **19**, 522–527 (2020).
- [21] Mong, R. S. K., Essin, A. M. & Moore, J. E. Antiferromagnetic topological insulators. *Phys. Rev. B* **81**, 245209 (2010).
- [22] Li, J. *et al.* Magnetically controllable topological quantum phase transitions in the antiferromagnetic topological insulator MnBi_2Te_4 . *Phys. Rev. B* **100**, 121103 (2019).
- [23] Chen, Y. J. *et al.* Topological electronic structure and its temperature evolution in antiferromagnetic topological insulator MnBi_2Te_4 . *Phys. Rev. X* **9**, 041040 (2019).
- [24] Hu, C. *et al.* A van der Waals antiferromagnetic topological insulator with weak interlayer magnetic coupling. *Nat. Commun.* **11**, 97 (2020).
- [25] Ma, J. *et al.* Emergence of nontrivial low-energy Dirac fermions in antiferromagnetic EuCd_2As_2 . *Adv. Mater.* **32**, 1907565 (2020).
- [26] Gao, A. *et al.* Layer Hall effect in a 2D topological axion antiferromagnet. *Nature* **595**, 521–525 (2021).
- [27] Huan, S. *et al.* Multiple Magnetic Topological Phases in Bulk van der Waals Crystal MnSb_4Te_7 . *Phys. Rev. Lett.* **126**, 246601 (2021).
- [28] Zhang, Z. *et al.* Controlled large non-reciprocal charge transport in an intrinsic magnetic topological insulator MnBi_2Te_4 . *Nat. Commun.* **13**, 6191 (2022).
- [29] Monso, S. *et al.* Crossover from in-plane to perpendicular anisotropy in Pt/CoFe/AlO_x sandwiches as a function of Al oxidation: A very accurate control of the oxidation of tunnel barriers. *Appl. Phys. Lett.* **80**, 4157–4159 (2002).
- [30] Rodmacq, B., Auffret, S., Dieny, B., Monso, S. & Boyer, P. Crossovers from in-plane to perpendicular anisotropy in magnetic tunnel junctions as a function of the barrier degree of oxidation. *J. Appl. Phys.* **93**, 7513–7515 (2003).
- [31] Dieny, B. & Chshiev, M. Perpendicular magnetic anisotropy at transition metal/oxide interfaces and applications. *Rev. Mod. Phys.* **89**, 025008 (2017).
- [32] Li, B. *et al.* Quasi-two-dimensional ferromagnetism and anisotropic interlayer couplings in the magnetic topological insulator MnBi_2Te_4 . *Phys. Rev. B* **104**, L220402 (2021).
- [33] Sass, P. M., Kim, J., Vanderbilt, D., Yan, J. & Wu, W. Robust A-type order and spin-flop transition on the surface of the antiferromagnetic topological insulator MnBi_2Te_4 . *Phys. Rev. Lett.* **125**, 037201 (2020).
- [34] Ge, W. *et al.* Direct visualization of surface spin-flip transition in MnBi_4Te_7 . *Phys. Rev. Lett.* **129**, 107204 (2022).
- [35] Chang, C.-Z. *et al.* High-precision realization of robust quantum anomalous Hall state in a hard ferromagnetic topological insulator. *Nat. Mater.* **14**, 473 (2015).
- [36] Ou, Y. *et al.* Enhancing the quantum anomalous Hall effect by magnetic codoping in a topological insulator. *Adv. Mater.* **30**, 1703062 (2018).
- [37] Mills, D. L. Surface spin-flop state in a simple antiferromagnet. *Phys. Rev. Lett.* **20**, 18–21 (1968).
- [38] Yang, S. *et al.* Odd-even layer-number effect and layer-dependent magnetic phase diagrams in MnBi_2Te_4 . *Phys. Rev. X* **11**, 011003 (2021).
- [39] Ovchinnikov, D. *et al.* Intertwined topological and magnetic orders in atomically thin Chern insulator MnBi_2Te_4 . *Nano Lett.* **21**, 2544–2550 (2021).

- [40] Chong, S. K. *et al.* Intrinsic exchange biased anomalous Hall effect in an uncompensated antiferromagnet MnBi_2Te_4 . *Nat. Commun.* **15**, 2881 (2024).
- [41] Brown, W. F. Virtues and weaknesses of the domain concept. *Rev. Mod. Phys.* **17**, 15–19 (1945).
- [42] Aharoni, A. Theoretical search for domain nucleation. *Rev. Mod. Phys.* **34**, 227–238 (1962).
- [43] Hug, H. J. *et al.* Quantitative magnetic force microscopy on perpendicularly magnetized samples. *J. Appl. Phys.* **83**, 5609–5620 (1998).
- [44] Parker, G. W. Electric field outside a parallel plate capacitor. *Am. J. Phys.* **70**, 502–507 (2002).
- [45] Kim, D.-H., Choe, S.-B. & Shin, S.-C. Direct observation of Barkhausen avalanche in Co thin films. *Phys. Rev. Lett.* **90**, 087203 (2003).
- [46] Schwarz, A. *et al.* Visualization of the Barkhausen effect by magnetic force microscopy. *Phys. Rev. Lett.* **92**, 077206 (2004).
- [47] Lachman, E. O. *et al.* Observation of superparamagnetism in coexistence with quantum anomalous Hall $C = \pm 1$ and $C = 0$ Chern states. *npj Quantum Mater.* **2**, 70 (2017).
- [48] Wang, W. *et al.* Direct evidence of ferromagnetism in a quantum anomalous Hall system. *Nat. Phys.* **14**, 791 (2018).
- [49] Shi, Y. *et al.* Correlation between magnetic domain structures and quantum anomalous Hall effect in epitaxial MnBi_2Te_4 thin films. *Phys. Rev. Mater.* **8**, 124202 (2024).
- [50] Tschirhart, C. L. *et al.* Imaging orbital ferromagnetism in a moiré chern insulator. *Science* **372**, 1323–1327 (2021).
- [51] Redekop, E. *et al.* Direct magnetic imaging of fractional Chern insulators in twisted MoTe_2 . *Nature* **635**, 584–589 (2024).
- [52] Sun, Z. *et al.* Resolving and routing magnetic polymorphs in a 2D layered antiferromagnet. *Nat. Mater.* **24**, 226–233 (2025).
- [53] Yang, S. *et al.* Defect-assisted domain nucleation drives unique exchange-bias phenomena in MnBi_2Te_4 . *Phys. Rev. X* **14**, 041024 (2024).
- [54] Chen, B. *et al.* Even-odd layer-dependent exchange bias effect in MnBi_2Te_4 Chern insulator devices. *Nano Lett.* **24**, 8320–8326 (2024).